Acta Materialia 285 (2025) 120646

Contents lists available at ScienceDirect

Acta Materialia

journal homepage: www.elsevier.com/locate/actamat

Full length article

Acoustic profiling of intermittent plasticity

Mostafa M. Omar, Jaafar A. El-Awady *

Department of Mechanical Engineering, Johns Hopkins University, 3400 N. Charles St., Baltimore, 21218, MD, USA

ARTICLE INFO

Keywords:
Dislocations
Acoustic emissions
Plasticity
In situ microcompression testing

ABSTRACT

Unraveling the complexities of metal deformation requires a deep understanding of dislocation dynamics and their intermittent behavior. Here, high-resolution acoustic emissions (AE) measurements during *in situ* microcompression of Ni single-crystal micropillars are used to reveal new insights into the rapid deformation dynamics of dislocation avalanches. Spectral analysis of the AE signals uncovers multiple short waves during individual strain bursts, exposing a rich landscape of intermittent plasticity that was previously hidden. Our analysis identifies distinct acoustic signatures that correlate with various stages of deformation: early-stage large avalanches generate strong AE bursts, while later stages characterized by denser dislocation networks emit AE signals of lower amplitude. Notably, given the used sensor, a consistent AE frequency band ranging from 30 to 50 kHz is observed across all recorded avalanches, directly linking this spectral feature to the kinematics of dislocations moving through the crystal lattice. These findings provide a non-destructive characterization approach of dislocation dynamics during the deformation of bulk metals and establish quantitative connections between defect dynamics and macroscopic deformation behavior. More broadly, this work highlights the potential for AE-based techniques to provide insights into the fundamental mechanisms of plasticity in crystalline materials.

1. Introduction

In crystalline materials, plastic deformation is governed by the microscopic dynamics of dislocations – linear defects that glide due to the slip of atoms through the lattice – allowing a solid to permanently change its shape (i.e., plastically deform). As metals deform, dislocations multiply, interact, and self-organize into complex structures, controlling a remarkable diversity of mechanical, magnetic, optical, and electric properties [1–5]. Hence, there is a dire need to link macroscale plastic flow to the microscopic dynamics of these dislocations [6].

The hallmark of plasticity at the microscale is its intermittent nature [7]. This behavior results from the rapid motion of groups of dislocations, known as dislocation avalanches. The classical ways of studying avalanches' dynamics relying on studying the far-field variables, such as stress and strain, have resulted in significant understanding of intermittent plasticity [8–13]. Nevertheless, the far-field mechanical response represents an ensemble average of local contributors (e.g., dislocations motion, cracks initiation or propagation) throughout the material volume [14,15]. Therefore, gaps remain in understanding the underlying mechanisms using these methods owing to the temporal overlap of different mechanisms, and to the low resolution (ms) – which are usually associated with mechanical instruments – compared to the fast dynamics occurring on microseconds timescale [16].

Fortunately, when activated, these local contributors produce sudden local changes in the elastic strain, generating high-frequency elastic stress waves in the material known as acoustic emissions (AE) [17]. These waves can be detected using surface piezoelectric sensors at a sub-microsecond resolution. Hence, AE can provide access to previously elusive intermittent plasticity dynamics. In addition, the features of these waveforms are source-dependent, allowing the decoupling of temporally overlapped deformation activities [18–24]. However, applying this technique to investigate the microscale behavior of metals poses challenges due to the low signal-to-noise ratio (SNR), making it difficult to distinguish genuine waves from background noise. As a result, only a few attempts were presented in recent literature [25,26]. Yet, these reports did not make use of the full potential of the AE capabilities, e.g., spectral analysis.

In this study, we synergistically combine high-resolution AE measurements with *in situ* scanning electron microscopy (SEM) microcompression of Ni single-crystal micropillars. By directly measuring AE during deformation, we aim to unravel the complex interplay between dislocation dynamics, stress redistribution, and their AE features at an enhanced temporal resolution compared to previous studies [12, 27–30]. By correlating the distinct features of the AE signals with the dislocation activities inferred from the concurrent stress–strain

* Corresponding author.
E-mail address: jelawady@jhu.edu (J.A. El-Awady).

https://doi.org/10.1016/j.actamat.2024.120646
Received 21 August 2024; Received in revised form 5 November 2024; Accepted 8 December 2024
Available online 15 December 2024

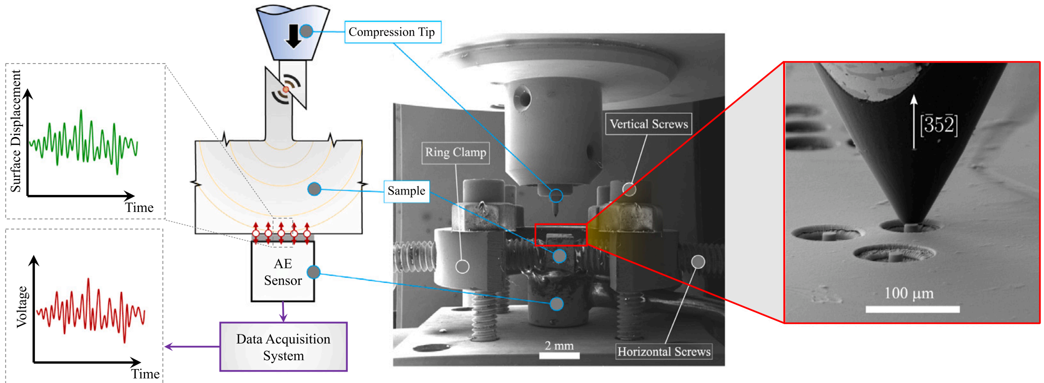

Fig. 1. A schematic and a real image showing the used experimental setup. The actuator moves the diamond tip to compress the micropillar. Once the micropillar starts deforming, AE waves are generated causing surface displacements. The AE sensor detects these surface displacements and converts them into a voltage signal. The inset to the right shows the flat-ended conical diamond tip as well as micropillars that were FIB milled into the top surface of the sample.

response, we can establish unique acoustic signature characteristics of different deformation stages.

2. Material and methods

2.1. Material

The material used in this study is a single-crystal Nickel (Ni) with 99.999% purity obtained from Goodfellow Corporation, USA. The obtained Ni bar was cut into a cuboidal specimen with dimensions $3.3 \times 3.3 \times 9.0$ mm^3 using wire electrical discharge machining (EDM). One of the cuboids was then mechanically polished to a 6 μm finish on all sides with metallurgical paper, then heat treated at a temperature of 1365 °C in Argon at a back pressure of 1 psi for 2 weeks to reduce the initial dislocation density in the material, resulting in an initial dislocation density of 3.75×10^8 m^{-2} [10].

The cuboidal specimen was then sectioned using wire EDM to produce a parallel-sided sample with its top surface having a plane normal parallel to the $[\bar{3}5\bar{2}]$ crystallographic direction. The top surface of the parallel-sided sample was then mechanically polished, and electropolished to remove any damage. All details of the thermal annealing and polishing are described in [10].

2.2. Micropillar fabrication

Micropillars were fabricated into the top surface of the Ni parallel-sided sample for subsequent microcompression experiments. The micropillars were fabricated using the annular-milling technique with a Thermo Scientific Helios G4 UC Focused Ion Dual Beam (FIB) at 30 kV [31]. This is a multi-step procedure in which trenches with rough edges are first fabricated using a large beam current (47 nA), then the current is gradually decreased as the micropillar geometry approaches the desired final geometry. The final FIB milling was performed at a beam current of ≤ 2.5 nA. This approach was chosen to minimize tapering, Ga-ion damage in the near-surface region of the micropillar, and to achieve a higher accuracy finish.

Micropillars with 10 μm diameter, referred to hereafter as the D10 were fabricated into the Ni sample top surface. For clarity, only three micropillars are discussed in this work, however, the rest of the micropillars followed similar trends. The fabricated micropillars had a taper angle less than 3° and a height-to-diameter aspect ratio of ≈ 3–3.3. The axis of all micropillars was oriented along the $[\bar{3}5\bar{2}]$ crystallographic direction as shown in Fig. S1. This was the loading direction used for all subsequent experiments. This orientation was chosen to achieve single-slip deformation under uniaxial compression loading. The Schmid factor for the associated primary slip system in this case is 0.45, while the next highest Schmid factor for other slip systems was 0.34.

2.3. Experimental setup

In situ uniaxial micropillar compression experiments were performed inside a Tescan Mira3 Scanning Electron Microscope (SEM) coupled with an acoustic emissions detection system. Fig. 1 shows a schematic for the experimental setup that was developed for this study. In the following, we summarize the micro-mechanical loading methodology and the acoustic emission sensing.

2.3.1. In situ micro-mechanical loading

The uniaxial micropillar compression experiments were conducted using a Nanomechanics (now a subsidiary of KLA Corporation) In-SEM cradle with an InForce 1000 actuator (1 N load cell), that is mounted on the SEM stage. The cradle has a micro-positioner stage on which the sample is mounted. The actuator is equipped with a conical-shaped diamond tip with a flat end having a 25 μm diameter that would interface with the top surface of the micropillars during the microcompression tests. The actuator was operated in a load-controlled mode with a loading rate of 0.16 mN/s and a data acquisition rate of 600 Hz. In the current load-controlled methodology, the applied loading rate on the specimen $\dot{F}_s$ equals the actuator-imposed rate $\dot{F}_i$ minus the rate overcoming instrument stiffness K_i, i.e., $\dot{F}_s = \dot{F}_i - K_i \dot{D}$, where $\dot{D}$ is the platen displacement rate. When a dislocation avalanche activates, the plastic strain rate scales with mobile dislocation density and velocity [32]. This results in a larger deformation rate in the micropillar, and subsequently increasing $\dot{D}$. During the avalanche, the higher $\dot{D}$ will result in a lower loading rate $\dot{F}_s$ in the micropillar. If the avalanche plastic strain rate is sufficiently high, $\dot{F}_s$ becomes negative and the stress decreases, which is commonly referred to as a stress drop [33]. Simultaneously, a jump is seen on the strain–time curve, referred to as a strain burst.

2.3.2. Acoustic emissions sensing

Acoustic emissions were recorded during the microcompression experiments using a commercial PICO piezoelectric sensor, 2/4/6 preamplifier, and a PCI-2-based data acquisition system available from Physical Acoustics Corporation (Mistras).

To couple the AE detection with the *in situ* micropillar experiments, various modifications had to be made to the conventional AE measurements for bulk experiments. In conventional AE setups, there is usually a large stimulus and various AE sources active at any given point in time. However, in the current experiments, the deformation being sensed is at a very localized region of the material. Also, the loads applied are relatively small (<50 mN). With this in mind, the AE sensor was mounted directly under the sample, which represents the most direct path for sensing the generated acoustic waves with minimum attenuation and without any interference with the electron beam used for imaging. To further reduce signal attenuation between the Ni bulk sample and the AE sensor, vacuum grease was applied between the sample and the sensor.

An ad-hoc fixture was used such that the AE sensor is fixed to both the InSEM cradle and the Ni sample. A custom ring clamp was designed to hold the sample in place from its side faces. In this way, the sample's bottom side can be in direct contact with the sensor throughout the experiment (see Fig. 1). This is achieved through a set of four horizontal screws in the ring to hold the sample from the side (away from the location of the micropillars) and the ring is then clamped to the InSEM cradle base through a set of four vertical screws.

Early experiments (not reported in this article) were performed using a Physical Acoustics HD2WD wide-band sensor. It was concluded from these experiments that the frequency ranges corresponding to deformation events were at low frequencies. Hence, a Physical Acoustics PICO sensor with a narrower bandwidth was selected to perform the experiments, aiming for a higher SNR. Note that the used sensor's resonance frequency is 460 kHz, as per the manufacturer data sheet.

AE waveforms were recorded with an acquisition rate of 2 MHz. Afterward, for the purposes of quantitative analysis, waveforms were converted to a "hit" construct using a Hit Definition Time (HDT) of 100 μs and Hit Lockout Time (HLT) of 10 μs. Details of conversion from waveform to hit-based construct can be found in the AE waveforms processing section. A preamplifier with a gain of 60 dB was used to amplify the signal before being read by the data acquisition board. To determine the noise threshold for each sample, different threshold values were tested, and the chosen one was the minimum such that no hits were captured during the elastic loading regime, i.e., just above the level of the background noise. The time synchronization between AE and InSEM systems is detailed in the Supporting Information Section 2. Table S1 in the Supporting Information summarizes the different parameters used in the data processing.

2.4. Data analysis

2.4.1. AE waveforms processing

AE waveforms were recorded during the experiments with no real-time processing. Next, the waveforms are processed using MATLAB to enhance the SNR ratio. Bandpass filtering is used to filter out the frequencies that constitute the major portion of the background noise and have minimal contribution during the deformation events.

To accurately define this narrow frequency range corresponding to deformation, the following procedures were performed sequentially. First, two segments of the waveform are extracted, one segment during the early elastic regime, where there is no presence of any bursts. Hence, the recorded signal is the overlap of waves from different noise sources (e.g., ambient noise of the SEM chamber and acquisition board noise). The second waveform segment is extracted out of a time interval around the waveform's peak amplitude during the experiment, i.e., at the time when the deformation activities are most active. Next, the power spectra of both signals are computed, plotted, and compared. Most of the power spectrum was found to overlap with minimal differences. This is expected since signals resulting from dislocation avalanches are very weak compared to the background noise. However, after subtracting the power spectrum of the pure noise signal from the one during the deformation events, we define a frequency range at which the two signals are significantly different, i.e., a frequency bandwidth that is dominant during deformation and absent in the pure noise waveform, see Fig. S5. Hence, this narrow range is selected to be the bandpass range. Fig. 2 shows the waveforms before and after filtering. The noise background amplitudes after filtering are lower, and weak spikes (highlighted with yellow arrows in the figure) are identified in the filtered signal which were formerly buried under the noise in the raw signal. The filtered waveforms were used for the quantitative analysis (e.g., AE energy and amplitude calculation) only. Raw waveforms were used in the spectral characterization of the deformation activities to avoid any influence from the bandpass filter.

To quantitatively analyze the waveform features, filtered waveforms are processed and transformed into a hit-based data set by using NOESIS software [34]. NOESIS is a software designed for advanced acoustic emission data analysis, pattern recognition, and neural networks, developed by Mistras Group Hellas ABEE, Athens, Greece. The version used for all the analyses in this work was NOESIS Essential 9.0.

A hit is a portion of the detected waveform when the waveform amplitude exceeds a predetermined threshold. This threshold is chosen to be above the noise level to avoid incorporating noise signals in the subsequent analyses. In this work, the threshold for detecting AE hits was set to minimize false hit detection during elastic deformation. As a result, multiple threshold values were tested, and the selected threshold is the lowest value that does not register any hits during the elastic loading phase. Several acquisition parameters should be determined to transform the waveform into a hit-based data set. These parameters are Hit Definition Time (HDT), Peak Definition Time (PDT), Hit Lockout Time (HLT), and the threshold. The process of hit recording operates as follows. When the sensor detects a signal that surpasses the predefined threshold, a hit is triggered, initiating the recording process. As the signal reaches its maximum amplitude, the system waits for the PDT. If a higher amplitude is detected before the PDT elapses, it is recorded as the new maximum, and the system resets the PDT. If no further peaks are detected within this period, the current peak is registered as the peak amplitude. Following each threshold crossing, the system enters the HDT phase. If no additional crossings occur during this time, the last recorded time is marked as the end of the hit. Subsequently, the system enters the HLT phase, during which it temporarily stops signal acquisition until the next threshold crossing is detected. Hence, the "hit" construct helps resolve different events given that they have a temporal "silent" period in between, i.e., a period at which the wave amplitudes do not exceed the threshold. Once the waveform corresponding to a hit is extracted, various features of the wave can be calculated and stored in a tabulated format for further analysis.

2.4.2. InSEM bursts identification

Strain bursts are manifested as sudden stress drops in the stress–time curve and sudden strain jumps in the strain–time curve. A MATLAB script was developed to detect and analyze these strain bursts autonomously. The script relied on identifying the start and the end of the bursts from the stress drops on a filtered stress–time curve. To avoid the influence of the instrument noise on the stress drops' identification process, a minimum threshold was determined. Only the stress drops with a magnitude larger than this threshold were considered for analysis. The minimum threshold was determined as follows: The linear regime in the stress–time curve was extracted and fitted to a straight line. Next, the fitted line is subtracted from the raw data, and the stress variation range around the fitted line is calculated. This was considered as the instrument noise floor during the test. The threshold was taken to be higher than the instrument noise, which was 0.05 MPa for all micropillars.

2.4.3. Binning AE hits to InSEM strain bursts

Fig. 3 shows the binning of the AE hits with respect to their corresponding strain bursts. Due to the significant differences in the acquisition rates between the InSEM actuator and the AE system, multiple hits in the AE data set can fall within a single strain burst. The shaded area in the figure highlights the start and end of the strain burst as computed from the stress–time curves. AE hits that fell within the highlighted regions were binned together as a single point as follows: The time of the binned hit was selected to match the mean time of the strain burst; the hits' AE energies were summed together, while the amplitude of the binned hit was calculated as the maximum amplitude of all the original hits. However, some hits fell outside the strain bursts' intervals. Those hits likely correspond to small events that were not

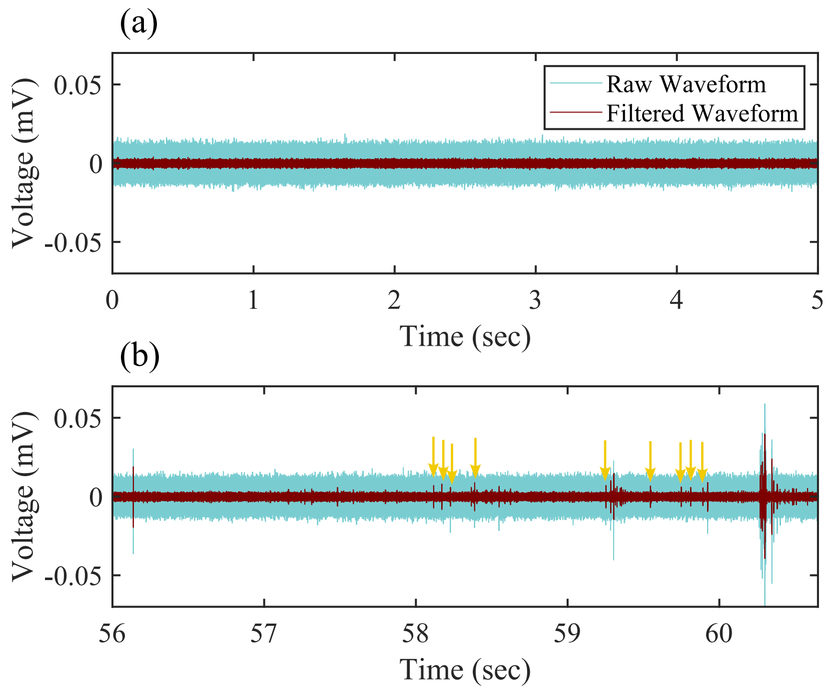

Fig. 2. Waveform filtering examples. (a) A noise waveform before and after filtering. (b) A waveform excerpt during the experiment before and after filtering. The yellow arrows highlight the peaks that were buried under the background noise and appeared after the filtering process. (For interpretation of the references to color in this figure legend, the reader is referred to the web version of this article.)

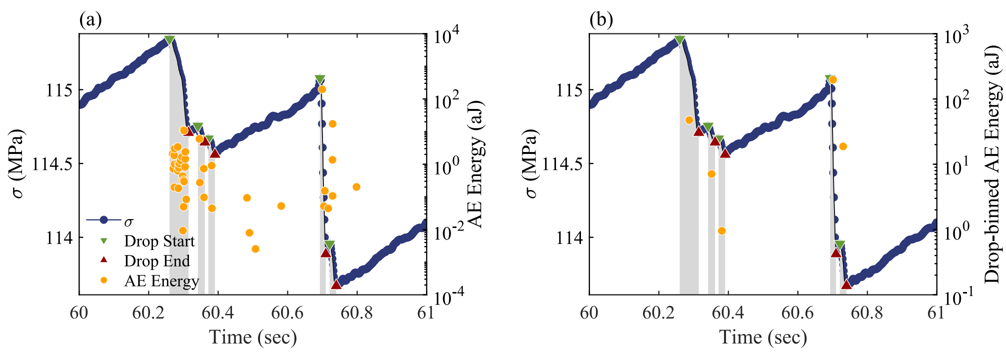

Fig. 3. AE hits binning. (a) AE hits before binning where many hits can be seen within a single drop. (b) AE hits after binning where every drop has one value for the AE energy.

detected by the InSEM system. Therefore, those hits were discarded in the analysis of the correlation between the AE and InSEM features. The percentage of the sum of the AE hits' energies that fell inside the strain burst intervals compared to the sum of all AE hits' energies was 85 ± 7%. This high percentage was considered as a verification of the effectiveness of the binning procedures.

The definitions of the different AE and InSEM terms and variables used in the following section can be found in the next section.

2.4.4. Definitions

All AE parameter definitions and calculations are from the NOESIS software manual [34].

- Burst Velocity (μm/s): Average platen velocity of the actuator during the strain burst.

  $$v = \Delta D/\Delta t$$

  where v is the burst velocity, ΔD is the vertical displacement moved by the actuator during the burst, and Δt is the burst duration.
- Resolved Burst Velocity (μm/s): the average velocity of the burst on the slip plane.

  $$v_r = \Delta D_r/\Delta t$$

  where v_r is the resolved burst velocity, ΔD_r is the displacement moved by a burst on the slip plane, and Δt is the burst duration.
- Exit Dislocation Rate (kHz): the rate of dislocations exiting the surface of the micropillar during an avalanche as calculated as follows:

  $$\frac{S}{b \cdot \Sigma t_{AE}}$$

  where S is the burst magnitude, b is the Burgers vector magnitude, and Σt_{AE} is the sum of the durations of the AE hits during the avalanche. Σt_{AE} was used instead of Δt of the avalanche as measured from the loading instrument to make use of the enhanced acquisition rate of the AE system.
- AE Energy (aJ): True energy of the signal on a 10 kΩ resistor computed at the sensor.

  $$E_{AE} = \frac{10^{12}}{R \cdot SF \cdot 10^{2 \cdot \frac{G}{20}}} \cdot \sum_i [V(i)]^2$$

  where E_{AE} is the energy, R is the resistor in Ohms, SF is the sampling frequency in MHz, G is the pre-amp gain in dB (60 in

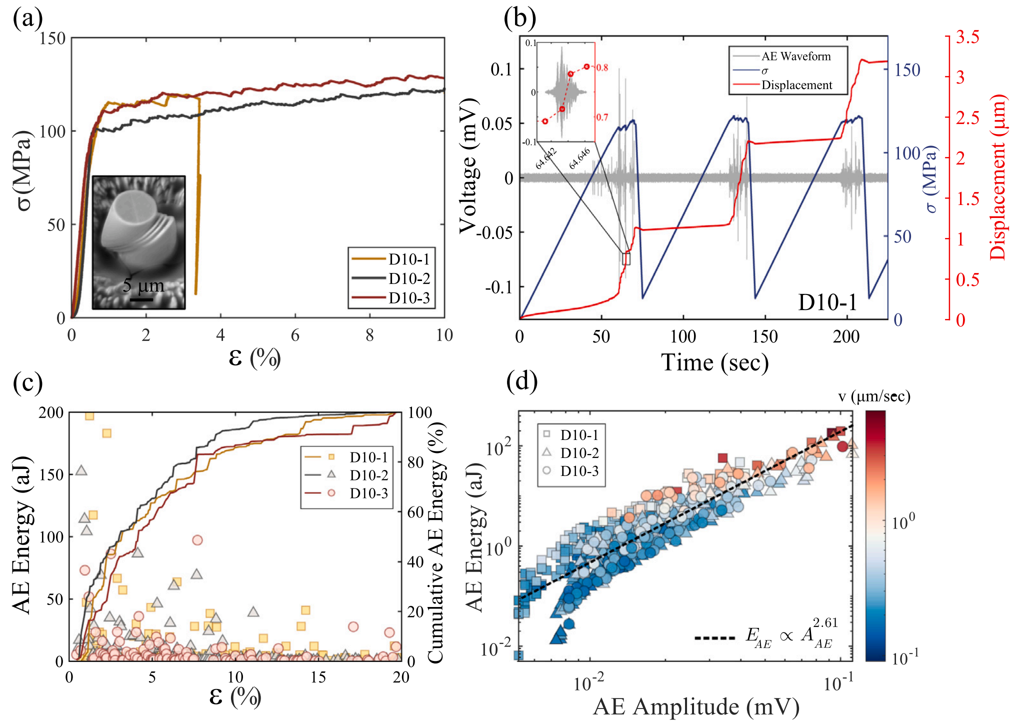

Fig. 4. The mechanical and acoustic response of Ni single-crystal micropillars during microcompression deformation. (a) The stress–strain curves of tested D10 micropillars. The numbers after the micropillar size in the caption indicate the micropillar number. The inset shows an SEM micrograph of the D10-1 deformed micropillar, showing the single-slip response, which is a representative morphology of all the tested micropillars. (b) The displacement, stress, and the corresponding recorded AE filtered waveform versus time for the D10-1 micropillar. The inset shows a single displacement burst, which was active throughout ≈ 5 ms, to highlight the significant difference in the acquisition rates of both measurement systems. (c) The measured AE hit energy versus strain. The symbols represent the binned AE hit energies, while the solid lines represent the cumulative sum of the AE energy. (d) The measured AE energy versus AE amplitude for the tested micropillars. The symbols are color-coded according to the platen velocity as shown in the legend, and the dashed line is the fitted line for all data points. (For interpretation of the references to color in this figure legend, the reader is referred to the web version of this article.)

all the experiments), and $V(i)$ is the sample point amplitude at pre-amplifier output (i.e., as is in the data file) in Volts.

- AE Amplitude (mV): Maximum absolute value of the waveform voltage signal during the hit.
- Peak Frequency (kHz): The frequency corresponding to the peak value in the power spectrum obtained from the FFT (Fast Fourier Transform) of the waveform.

3. Results and discussion

3.1. Temporal correlation of stress–strain response and acoustic emission bursts

The stress–strain curves of the deformed micropillars are shown in Fig. 4(a). After the onset of yield, the serrated curves reflect the intermittent behavior resulting from sudden slip bursts as the micropillars deform. The inset shows a representative postmortem SEM micrograph of one of the deformed micropillars. All the observed slip traces are on $(\bar{1}11)$ planes, indicating that the desired single-slip deformation was achieved. The stress versus time, platen displacement versus time, and the corresponding AE signal curves for the D10-1 micropillar are shown in Fig. 4(b). These are representative of all tested micropillars with the exception that the D10-1 micropillar was unloaded every 3.3% strain to rule out any loading setup effects on the measured AE. The recorded AE signal is composed of high-amplitude intermittent bursts superimposed on a low-amplitude continuous background. The background noise originates from different inevitable sources, including the sensor wires and the acquisition board [35]. In contrast, the high-amplitude bursts are associated with the intermittent activation of dislocation avalanches [17,26]. However, several possibilities exist for the source of these AE waves.

The AE signals can originate not only from deformation activities but also from multiple sources, such as background noise or the moving parts of the loading instrument. The loading/unloading every 3.3% strain experiment was performed to investigate the contribution of the potential sources other than the deformation of the micropillars (see Supporting Material Video 1). As depicted in Fig. 4(b), no amplitude bursts are seen till the deviation from the linear elastic regime, then as the displacement bursts start, the AE bursts start showing up. Afterward, during unloading and reloading, no AE bursts were detected – even though the actuator was moving and changing its direction – until the moment when the stress drops started once again, i.e., a new deformation event. Moreover, these high amplitude waves synchronize perfectly with the stress drops in the stress–time plots as shown in Fig. S2, matching the physical interpretation for the expected sources of AE waves. This synchronization between the AE bursts and displacement bursts shows that the AE technique is capable of detecting the rapid dislocation dynamics associated with intermittent plasticity. Lastly, since the micropillars are compressed in a single-slip orientation, no other deformation mechanisms are expected to be active during deformation other than dislocation avalanches.

Classically, the statistics of dislocation avalanches were computed by analyzing the displacement bursts or load drops as measured from the loading instrument [12,27–30,36]. These techniques capture the far-field temporal average response of the samples without addressing the individual microscopic events. The inset in Fig. 4(b) highlights the strength of augmenting conventional microcompression testing with the AE technique in addressing the complexities of studying intermittent plasticity. The inset shows a strain burst and the limited temporal resolution of mechanical loading instruments (acquisition rate of 600 Hz or a data point every 1.66 ms) as compared to high-bandwidth AE system (acquisition rate of 2 MHz, corresponding to a data point every 0.5 μs). For the shown strain burst, the mechanical instrument

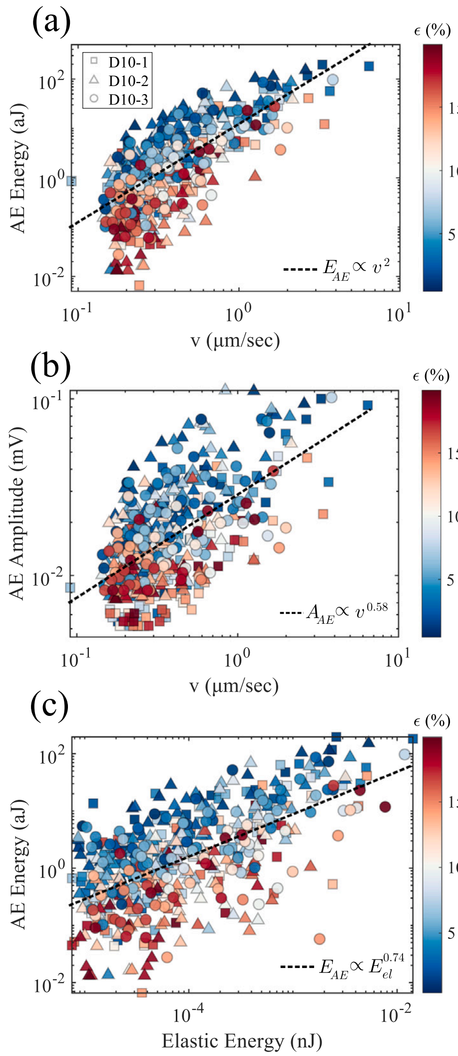

Fig. 5. Correlating acoustic emission features with deformation burst kinetics. A scatter plot of the: (a) AE energy during strain bursts versus the burst velocity; (b) Maximum AE hits amplitude during strain bursts versus the burst velocity; and (c) The AE hits energy as a function of the released elastic energy during the strain bursts. The dashed lines represent the overall fit of all the micropillars data. Each data point is also colored according to the strain at which it was detected as shown by the color bar to the right of each figure. (For interpretation of the references to color in this figure legend, the reader is referred to the web version of this article.)

was able to sample only three data points, showing a monotonic increase of displacement during this event. In contrast, the AE system collected approximately 10^4 data points within the same time span ($\approx$ 5 ms) displaying several excitations with varying amplitudes. This enhanced temporal resolution facilitates a more insightful investigation of the intermittent plasticity phenomena as will be discussed below.

3.2. Dislocation avalanche characteristics from quantitative analysis of the acoustic emission waveforms

To quantify the dislocation avalanche characteristics from the AE waveforms analysis, the measured AE waveforms are converted into a “hit” construct, and the energy and amplitude of each hit is calculated as detailed in the data analysis section.

Fig. 4(c) summarizes the measured AE energy of the detected hits versus strain for the tested samples. The overall behavior for the different micropillars is nearly equivalent; the peak AE energies are measured at low strain values, and as deformation increases, the peak AE energy decreases. This trend is also evident from the cumulative AE energy curves, which show a decreasing slope with increasing strain for strains ≤ 10%, after which the curve nearly plateaus. This limit closely aligns with findings in the literature, which indicate that substantial densities are present on slip traces after only 11% shear strain, and that these structures do not undergo significant changes at higher strains. This suggests that much of the critical dislocation activity takes place early in the deformation process [37]. The measured AE amplitudes exhibit a similar trend, with the highest AE amplitudes recorded at early strains, then decreasing with increasing strains (see Supporting Information Fig. S3(a)).

Fig. 4(d) shows the AE energy versus the AE amplitude of binned AE hits during each strain burst, along with the associated platen average velocity during the same strain burst, hereafter referred to as burst velocity. The relationship between the AE energies, E_{AE}, and AE amplitudes, A_{AE}, was consistent across the tested micropillars, with the E_{AE} increasing along with the increase in A_{AE}. The relationship between E_{AE} and A_{AE}, can be described by a power law of the form $E_{AE} \propto A_{AE}^{2.61}$.

Figs. 4(c) and (d) also reveal that the dislocation avalanches producing the fastest strain bursts tend to originate at early stages of deformation. These fast avalanches also generate the strongest AE waves, as evidenced by the higher AE energies and amplitudes associated with these events (see Supporting Information Fig. S3(b) for additional details). This observation suggests that the early stages of plastic deformation, where mobile dislocation densities are relatively low and interactions are less frequent, are characterized by more energetic and rapid dislocation avalanches, which can be effectively captured by the high-resolution AE technique.

The observed decay in the peak AE energy with increasing strain provides supporting evidence for some of the classical phenomenological models of AE from dislocation activities, such as dislocation glide, acceleration/deceleration, multiplication, annihilation, pinning and unpinning mechanisms [17,38–58]. Despite the differences in the functional forms and constants used in these models, they broadly suggest that the AE amplitude scales directly with dislocation velocity, while AE energy scales with the square of velocity (*cf.* [50,54,56,57,59–62]). This qualitatively aligns with our observation that the highest AE energies and amplitudes are those associated with highest burst velocities.

Furthermore, to quantitatively compare the current results with these phenomenological models, direct comparisons between the AE features and the burst velocities are shown in Fig. 5. Generally, the results of all micropillars overlap and show a clear positive correlation between both the AE energies and amplitudes with the burst velocities. Fig. 5(a) shows the binned AE hits energy versus burst velocity for the different micropillars. A large scatter can be seen which can be expected given the low SNR. However, the data can be fitted to a power law equation in the form of $E_{AE} \propto v^{2\pm0.2}$ ($R^2 = 0.5$), which is in agreement with the model proposed by Miguel et al. suggesting that $E_{AE} \propto v_c^2$, where v_c is the collective velocity of moving dislocations [56].

Additionally, Fig. 5(b) shows the maximum AE amplitude during a strain burst versus the burst velocity. The data can be fitted to a power law equation with an exponent of 0.58 ± 0.15 ($R^2 = 0.4$), which is lower than the unity exponent proposed by the models suggesting that $A_{AE} \propto v$ [57]. Finally, the AE energy versus the released elastic strain energy, E_{el}, as calculated from the load–displacement curves for each strain burst, is shown in Fig. 5(c). The best fit for the data was a power law equation with an exponent of 0.74 ± 0.15 ($R^2 = 0.4$). This is also slightly different than earlier models in the literature that suggest a linear relationship following $E_{AE} = \alpha_{AE} E_{el}$, where α_{AE} is a scaling factor [55].

These slight discrepancies between the experimentally calculated exponents and those in the phenomenological models can be attributed to different factors. First, given the wide frequency spectrum of the generated waves and the limited bandwidth of the sensor, not all the

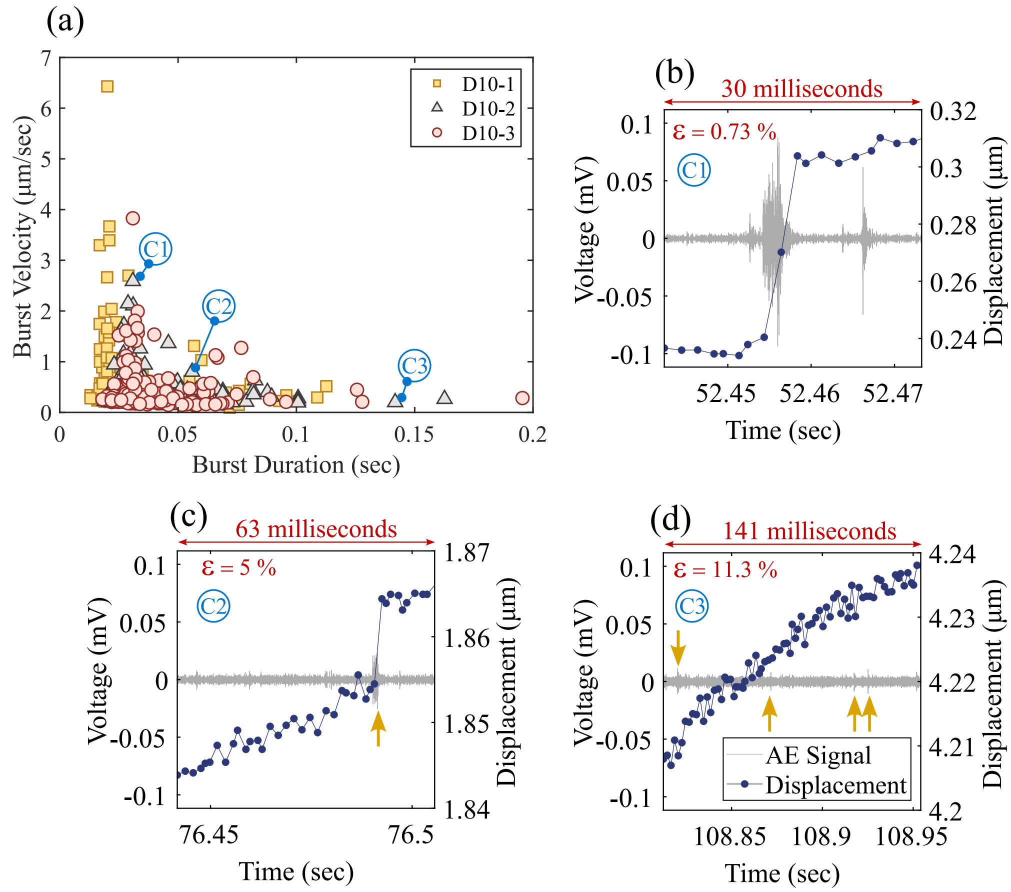

Fig. 6. Bursts classification. (a) A scatter plot for the burst velocity as a function of the burst duration for all the tested micropillars. Representative segments of the raw waveforms and the burst displacements as a function of time for the three burst types: (b) C1-type, (c) C2-type, and (d) C3-type. The three examples shown in (b)–(d) are from the D10-2 micropillar and are at 0.73%, 5%, and 11.3% strain, respectively.

emitted waves are recorded, i.e., lower total energies are measured compared to the energy emitted from the source. In addition, owing to the interaction between the elastic waves and dislocation forests that evolve as the micropillars are deformed, lower energies are expected to be measured with increasing strain [39,63,64]. Moreover, as mentioned earlier, different functional forms and constants were proposed in the literature for various dislocation activities that may temporally overlap, leading to an increased scatter. Lastly, the velocity term used in the theoretical models is the actual dislocation velocity, which is different than the average dislocation velocity or the burst velocity [65], which is used in the current analysis.

These factors collectively contribute to the observed discrepancies between the experimental results and the phenomenological model predictions. Despite these limitations, the overall agreement in the scaling trends of AE energy and amplitude with burst velocity and released elastic energy highlights that the AE technique can capture the essential features of dislocation dynamics during plastic deformation and can provide valuable insights into the dislocation dynamics. Future studies may address these limitations by employing more advanced signal processing techniques, using multiple sensors with wider bandwidth, and developing methods for directly measuring dislocation velocities during deformation.

It is also observed in Fig. 5 that the scatter in the AE energies spans one or two orders of magnitude for a given burst velocity range. Nevertheless, this scatter is not random. AE energies measured at lower strains (blue markers) are consistently higher than those measured at higher strains (red markers) for the same burst velocity values. This decay in energy with strain can be interpreted in light of the models proposing that $E_{AE} \propto \langle v\rangle^2 \rho_m \langle \Lambda\rangle$, where $\langle v\rangle$ is the average dislocation velocity, ρ_m is the mobile dislocation density in the avalanche, and $\langle \Lambda\rangle$ is the mean free path of the dislocations [66]. Both ρ_m and $\langle \Lambda\rangle$ decrease with increasing strain [67]. Consequently, a decline in AE energy is anticipated with increasing strain, even if dislocation velocity remains constant. Therefore, the results reveal that burst velocity, released elastic energy, dislocations mean free path, and mobile dislocations density, all had a clear influence on the released AE energies.

3.3. Bursts classification based on their AE response

Further correlations between the AE waveforms and the burst features as a function of the deformation stage are summarized in Fig. 6. Fig. 6(a) shows the correlation between the burst velocity and the burst duration for all tested micropillars. It is interesting to note that fast bursts are always associated with short duration (denoted hereafter as C1-type bursts), while bursts with long duration are always slower (denoted hereafter as C3-type bursts). All other bursts display an intermediate range of velocities and duration (denoted hereafter as C2-type bursts). Representative AE signatures associated with each of these types are also shown in Figs. 6(b)–(d). The acoustic and mechanical response of each of these three burst types reflects different signatures associated with the different stages of deformation.

At early deformation stages, when dislocation interactions are relatively weak, sudden movement of dislocation avalanches sweep large areas in short times, resulting in fast displacement bursts and strong AE waves, leading to distinct large displacement bursts and a sharp rise in AE wave amplitude over a short time (see Fig. 6(b)). With continued deformation of the micropillar, the formation of dislocation entanglements hinders the free motion of dislocations. Consequently,

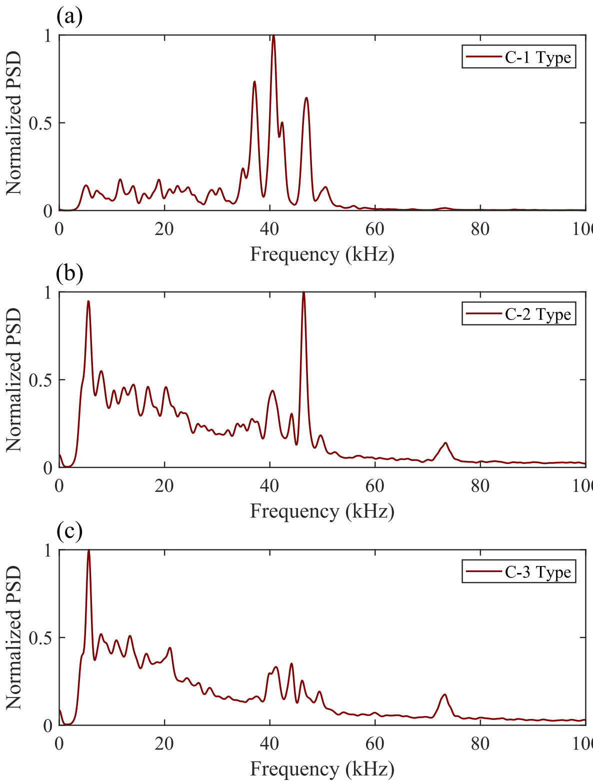

Fig. 7. Normalized Power Spectral Density (PSD) of the example bursts presented in Fig. 6. (a) C1-type, (b) C2-type, (c) C3-type. The y-axes of all plots were normalized with respect to their maximum power.

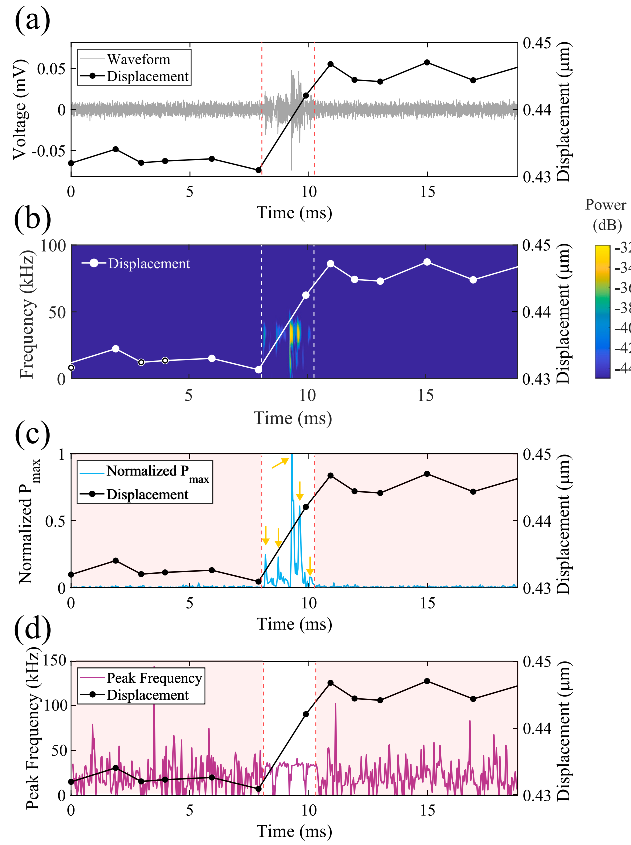

Fig. 8. Spectral insights into the rapid dislocation dynamics during strain bursts. (a) A representative raw waveform and the associated displacement versus time for a displacement burst from the D10-1 micropillar at a strain level of 1.3%. (b) A spectrogram of the waveform showing the frequency change as a function of time. The spectrogram was created using MATLAB "pspectrum" command with a 0.1 ms time resolution. (c) The normalized maximum power, P_{max}, among all frequencies as a function of time. The yellow arrows point to different peaks in power during the displacement drop, and the pink-shaded regions highlight areas where the power is ≈ 0 (indicating random noise). (d) The peak frequency in the waveform versus time. The x-axis is re-scaled in all figures to start after 60.7209 s on the absolute time scale of the experiment. The time was normalized here to highlight the short duration of the activity (≈ 3 ms). (For interpretation of the references to color in this figure legend, the reader is referred to the web version of this article.)

the emitted AE waves for C2-type bursts exhibit smaller AE amplitudes, less sharp rise in displacements, and longer duration compared to C1-burst type (see Fig. 6(c)). Here, the relative AE amplitudes are smaller than their C1 counterparts, indicating lower dislocation velocities [17]. At later stages of deformation, the extensive dislocation entanglements further reduce the dislocation mean free path and increase the attenuation of the signal [68,69]. Therefore, the lowest AE amplitudes and more gradual displacement rises are observed, as seen in Fig. 6(d). Hence, C3-type bursts exhibit significantly longer durations than C1- or C2-type bursts.

The differences in AE waves' frequency distributions between C1, C2, and C3 are highlighted in Fig. 7. The main difference is the relative power of the 30–50 kHz bandwidth compared to other frequency ranges. 30–50 kHz bandwidth is more dominant in C1-type bursts compared to C2 and C3. The significance of this bandwidth is discussed in the following section.

3.4. Acoustic emission spectral fingerprinting of dislocation avalanches during intermittent plasticity

Fig. 8 shows a representative unfiltered displacement versus time curve, the associated AE unfiltered waveform, and accompanying frequency analyses before, during, and after a single burst from the D10-1 micropillar. Note that, similar to the inset of Fig. 4(b), the displacement curve shows a single displacement burst event with only one displacement point measured during the burst event. On the other hand, the AE waveform reveals a clear intermittent behavior for this displacement burst. This intermittent behavior is characterized by the activation of multiple short AE bursts, see Fig. 8(a). This is further clarified in Fig. 8(b), where the spectrogram of the same waveform is plotted. Discrete and drastic changes in frequency powers can be seen, indicating the arrival of different signals with very short gaps in between. The relative change in the maximum power, P_{max}, within all frequencies versus time is shown in Fig. 8(c). Here, P_{max} is normalized with respect to the maximum value within this waveform excerpt. Notably, within less than 3 ms, five peaks were detected (labeled by yellow arrows in the figure). These peaks indicate the arrival of waves that dominate over the random noise baseline, which are characterized by zero or near zero power (see the regions shaded in pink in the figure). This observation indicates that the AE technique effectively resolved multiple events within a brief time interval, which appeared as a single event in the InSEM data. The spectral analysis of the peak frequency power reveals that these events exhibit varying magnitudes: they initially commence at a low magnitude, reach a peak, and subsequently decay before subsiding completely. This spectral behavior is likely to be associated with the kinematic processes of dislocation avalanches within the crystal lattice.

Furthermore, as shown in Fig. 8(d), these predominant waves maintain a nearly constant frequency in the range of 30–50 kHz bandwidth throughout the avalanche. Remarkably, this dominant peak frequency ranges between 10 and 80 kHz for all pillars tested and all avalanches detected, with the vast majority falling between 30 and 50 kHz as seen in Fig. 9(a), which is considerably far from the sensor's resonance frequency (≈ 460 kHz). A detailed investigation was performed to

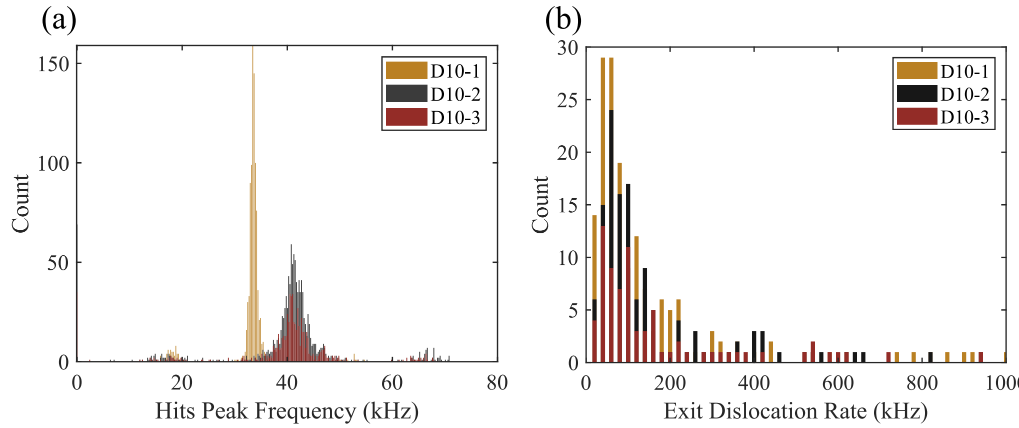

Fig. 9. Statistical distribution of Hits Peak Frequency and Exit Dislocation Rate. (a) Histogram of all the peak frequencies of the detected avalanches in all tested micropillars. Peak frequency is the frequency associated with the maximum power in the power spectrum of the avalanche waveform. (b) Histogram of the rate of dislocations exiting the surface of the micropillar during an avalanche.

ensure that this range is not an artifact of the sensor resonance or the sample resonance, see Supporting Information Section 3. This consistent frequency range for all avalanches suggests an inherent frequency signature of dislocation activities when avalanches are activated. This range aligns well with the rate of the dislocations exiting the surface during the bursts as shown in Fig. 9(b).

In addition, the average dislocation velocities can be correlated to the frequency spectrum of the recorded AE signals according to $\bar{v} = b \times \nu$, where ν is the AE wave predominant frequency [17]. For a frequency range of 10–50 kHz, the average dislocation avalanche velocity, $\bar{v}$, can be estimated to be in the range of 2.5–12.5 μm/s for Ni. This average dislocation avalanche velocity is in good agreement with the resolved avalanche burst velocity (i.e., the burst velocity on the active slip plane) for each avalanche as shown in Supporting Information Fig. S4. Future experimental, theoretical, and modeling efforts should be conducted to further quantify the origin of this unique frequency response during avalanches.

4. Conclusion

In this study, we utilized high-resolution acoustic emission measurements coupled with *in situ* SEM to unveil some of the elusive dynamics of dislocation avalanches during intermittent plasticity. By combining the temporal precision, frequency domain insights, and energy trends from measured AE signals, we have gained insights into the microscale dislocation dynamics that govern strain bursts in Ni micropillars. Our experimental results not only cross-validate phenomenological models previously proposed but also reveal new details of the complex dislocation processes that were previously hidden at conventional experimental time scale measurements. In particular, our results reveal distinct acoustic signatures for different stages of deformation, with large avalanches in the early stages emitting strong AE bursts, while denser dislocation networks at later stages produce lower-amplitude AE signals. Notably, given the used sensor, we have also identified a characteristic AE frequency band across all avalanches, which we link directly to the intrinsic dynamics of dislocations moving through the crystal lattice. Yet, while we believe this frequency range offers important insights into dislocation dynamics in our system, further research is necessary to assess its relevance across various materials and conditions. Future studies that examine how this frequency range varies with different experimental parameters could reveal a deeper understanding of dislocation motion and acoustic emission in crystalline materials.

Looking forward, we anticipate that high-resolution AE techniques will open new avenues for unraveling the complex physics of deformation and failure in a wide range of advanced materials, from nanostructured metals to high-entropy alloys and metallic glasses. Ultimately, the insights gained from listening to the acoustic response of materials may guide the design of novel microstructures with tailored mechanical properties, enabling new frontiers in materials engineering.

Funding sources

This research was sponsored by the National Science Foundation (NSF) under Grant No. 2225675.

CRediT authorship contribution statement

Mostafa M. Omar: Writing – review & editing, Writing – original draft, Visualization, Methodology, Investigation, Formal analysis. **Jaafar A. El-Awady:** Writing – review & editing, Supervision, Project administration, Methodology, Funding acquisition, Conceptualization.

Declaration of competing interest

The authors declare the following financial interests/personal relationships which may be considered as potential competing interests: Jaafar A. El-Awady reports financial support was provided by National Science Foundation. If there are other authors, they declare that they have no known competing financial interests or personal relationships that could have appeared to influence the work reported in this paper.

Acknowledgments

The authors would like to express their gratitude to Dr. Steven Lavestein for helping with the design of the experimental setup, Dr. Ahmed Barakat for fruitful discussions, and Prof. Peter Ispánovity for early discussions on reducing the noise level of the acoustic sensors.

Appendix A. Supplementary data

Supplementary material related to this article can be found online at https://doi.org/10.1016/j.actamat.2024.120646.

Data availability

Data will be made available on request.

References

[1] D. Hull, D.J. Bacon, Introduction to Dislocations, Elsevier, 2011, http://dx.doi.org/10.1016/C2009-0-64358-0.

[2] R. Ranjan, O. Buck, R.B. Thompson, A study on the effect of dislocation on the magnetic properties of nickel using magnetic NDE methods, J. Appl. Phys. 61 (8) (1987) 3196–3198, http://dx.doi.org/10.1063/1.338899.

[3] H.J. Queisser, E.E. Haller, Defects in semiconductors: Some fatal, some vital, Science 281 (5379) (1998) 945–950, http://dx.doi.org/10.1126/SCIENCE.281.5379.945/ASSET/01F2BF98-B2CB-4A63-9CAE-B50288A8D673/ASSETS/GRAPHIC/SE3486760007.JPEG.

[4] S. Nakamura, The roles of structural imperfections in ingan-based blue light-emitting diodes and laser diodes, Science 281 (5379) (1998) 956–961, http://dx.doi.org/10.1126/science.281.5379.956.

[5] C.H. Cho, H. Cho, Effect of dislocation characteristics on electrical conductivity and mechanical properties of AA 6201 wires, Mater. Sci. Eng. A 809 (2021) 140811, http://dx.doi.org/10.1016/J.MSEA.2021.140811.

[6] J.W. Hutchinson, Plasticity at the micron scale, Int. J. Solids Struct. 37 (1–2) (2000) 225–238, http://dx.doi.org/10.1016/S0020-7683(99)00090-6.

[7] D.M. Dimiduk, C. Woodward, R. LeSar, M.D. Uchic, Scale-free intermittent flow in crystal plasticity, Science 312 (5777) (2006) 1188–1190, http://dx.doi.org/10.1126/science.1123889.

[8] M.D. Uchic, D.M. Dimiduk, J.N. Florando, W.D. Nix, Sample dimensions influence strength and crystal plasticity, Science 305 (5686) (2004) 986–989, http://dx.doi.org/10.1126/science.1098993.

[9] J. Weiss, M.C. Miguel, Dislocation avalanche correlations, Mater. Sci. Eng. A 387–389 (1-2 SPEC. ISS) (2004) 292–296, http://dx.doi.org/10.1016/j.msea.2004.01.101.

[10] J.A. El-Awady, M.D. Uchic, P.A. Shade, S.L. Kim, S.I. Rao, D.M. Dimiduk, C. Woodward, Pre-straining effects on the power-law scaling of size-dependent strengthening in Ni single crystals, Scr. Mater. 68 (3–4) (2013) 207–210, http://dx.doi.org/10.1016/j.scriptamat.2012.10.035.

[11] J. Weiss, W.B. Rhouma, T. Richeton, S. Dechanel, F. Louchet, L. Truskinovsky, From mild to wild fluctuations in crystal plasticity, Phys. Rev. Lett. 114 (10) (2015) 105504, http://dx.doi.org/10.1103/PhysRevLett.114.105504.

[12] R. Maaß, M. Wraith, J.T. Uhl, J.R. Greer, K.A. Dahmen, Slip statistics of dislocation avalanches under different loading modes, Phys. Rev. E 91 (4) (2015) 42403, http://dx.doi.org/10.1103/PhysRevE.91.042403.

[13] J. Kacher, C. Kirchlechner, J. Michler, E. Polatidis, R. Schwaiger, H. Van Swygenhoven, M. Taheri, M. Legros, Impact of in situ nanomechanics on physical metallurgy, MRS Bull. 44 (06) (2019) 465–470, http://dx.doi.org/10.1557/mrs.2019.124.

[14] Y. Chen, B. Gou, D. He, X. Ding, J. Sun, E.K.H. Salje, Avalanche dynamics of dislocations and cracks under tension in additively manufactured copper, Appl. Phys. Lett. 124 (4) (2024) 42902, http://dx.doi.org/10.1063/5.0181702.

[15] Y. Chen, B. Gou, W. Fu, C. Chen, X. Ding, J. Sun, E.K.H. Salje, Fine structures of acoustic emission spectra: How to separate dislocation movements and entanglements in 316L stainless steel, Appl. Phys. Lett. 117 (26) (2020) 262901, http://dx.doi.org/10.1063/5.0030508.

[16] G. Sparks, R. Maaß, Shapes and velocity relaxation of dislocation avalanches in Au and Nb microcrystals, Acta Mater. 152 (2018) 86–95, http://dx.doi.org/10.1016/j.actamat.2018.04.007.

[17] J. Weiss, J.R. Grasso, Acoustic emission in single crystals of ice, J. Phys. Chem. B 101 (32) (1997) 6113–6117, http://dx.doi.org/10.1021/jp963157f.

[18] A. Vinogradov, K. Máthis, Acoustic emission as a tool for exploring deformation mechanisms in magnesium and its alloys in situ, JOM 68 (12) (2016) 3057–3062, http://dx.doi.org/10.1007/s11837-016-1966-2.

[19] S. Deschanel, W. Ben Rhouma, J. Weiss, Acoustic emission multiplets as early warnings of fatigue failure in metallic materials, Sci. Rep. 7 (1) (2017) 1–10, http://dx.doi.org/10.1038/s41598-017-13226-1.

[20] A. Vinogradov, D.L. Merson, The nature of acoustic emission during deformation processes in metallic materials, Low Temp. Phys. 44 (9) (2018) 930–937, http://dx.doi.org/10.1063/1.5052679.

[21] Y. Chen, K. Tang, B. Gou, F. Jiang, X. Ding, E.K.H. Salje, Acoustic emission spectra and statistics of dislocation movements in Fe40Mn40Co10Cr10high entropy alloys, J. Appl. Phys. 132 (8) (2022) 80901, http://dx.doi.org/10.1063/5.0098813.

[22] Y. Chen, B. Gou, B. Yuan, X. Ding, J. Sun, E.K. Salje, Multiple avalanche processes in acoustic emission spectroscopy: Multibranching of the energy-amplitude scaling, 2022, http://dx.doi.org/10.1002/pssb.202100465.

[23] Y. Chen, X. Ding, D. Fang, J. Sun, E.K.H. Salje, Acoustic emission from porous collapse and moving dislocations in granular Mg-Ho alloys under compression and tension, Sci. Rep. 9 (1) (2019) 1330, http://dx.doi.org/10.1038/s41598-018-37604-5.

[24] Y. Chen, B. Gou, X. Ding, J. Sun, E.K.H. Salje, Real-time monitoring dislocations, martensitic transformations and detwinning in stainless steel: Statistical analysis and machine learning, J. Mater. Sci. Technol. 92 (2021) 31–39, http://dx.doi.org/10.1016/j.jmst.2021.04.003.

[25] A.I. Hegyi, P.D. Ispanovity, M. Knapek, D. Tuzes, K. Mathis, F. Chmelik, Z. Dankhazi, G. Varga, I. Groma, Micron-scale deformation: A coupled in situ study of strain bursts and acoustic emission, Microsc. Microanal. 23 (6) (2017) 1076–1081, http://dx.doi.org/10.1017/S1431927617012594.

[26] P.D. Ispanovity, D. Ugi, G. Peterffy, M. Knapek, S. Kalacska, D. Tuzes, Z. Dankhazi, K. Mathis, F. Chmelik, I. Groma, Dislocation avalanches are like earthquakes on the micron scale, Nature Commun. 13 (1) (2022) 1975, http://dx.doi.org/10.1038/s41467-022-29044-7.

[27] J. Alcalá, J. Očenášek, J. Varillas, J.A. El-Awady, J.M. Wheeler, J. Michler, Statistics of dislocation avalanches in FCC and BCC metals: dislocation mechanisms and mean swept distances across microsample sizes and temperatures, Sci. Rep. 10 (1) (2020) 1–14, http://dx.doi.org/10.1038/s41598-020-75934-5.

[28] F.F. Csikor, C. Motz, D. Weygand, M. Zaiser, S. Zapperi, Dislocation avalanches, strain bursts, and the problem of plastic forming at the micrometer scale, Science 318 (5848) (2007) 251–254, http://dx.doi.org/10.1126/science.1143719.

[29] Y. Cui, G. Po, N. Ghoniem, Controlling strain bursts and avalanches at the nano-to micrometer scale, Phys. Rev. Lett. 117 (15) (2016) http://dx.doi.org/10.1103/PhysRevLett.117.155502.

[30] T. Richeton, J. Weiss, F. Louchet, Breakdown of avalanche critical behaviour in polycrystalline plasticity, Nature Mater. 4 (6) (2005) 465–469, http://dx.doi.org/10.1038/nmat1393.

[31] G.D. Sim, G. Kim, S. Lavenstein, M.H. Hamza, H. Fan, J.A. El-Awady, Anomalous hardening in magnesium driven by a size-dependent transition in deformation modes, Acta Mater. 144 (2018) 11–20, http://dx.doi.org/10.1016/j.actamat.2017.10.033.

[32] E. Orowan, Problems of plastic gliding, Proc. Phys. Soc. 52 (1) (1940) 8–22, http://dx.doi.org/10.1088/0959-5309/52/1/303.

[33] X. Zhao, D.J. Strickland, P.M. Derlet, M.R. He, Y.J. Cheng, J. Pu, K. Hattar, D.S. Gianola, In situ measurements of a homogeneous to heterogeneous transition in the plastic response of ion-irradiated ⟨111⟩ Ni microspecimens, Acta Mater. 88 (2015) 121–135, http://dx.doi.org/10.1016/j.actamat.2015.01.007.

[34] NOESIS™ - Advanced Data Analysis Pattern Recognition Software, https://www.physicalacoustics.com/by-product/noesis/.

[35] C.B. Scruby, An introduction to acoustic emission, J. Phys. E Sci. Instrum. 20 (8) (1987) 946–953, http://dx.doi.org/10.1088/0022-3735/20/8/001.

[36] S. Papanikolaou, Y. Cui, N. Ghoniem, Avalanches and plastic flow in crystal plasticity: an overview, Model. Simul. Mater. Sci. Eng. 26 (1) (2018) 013001, http://dx.doi.org/10.1088/1361-651X/aa97ad.

[37] D.M. Norfleet, D.M. Dimiduk, S.J. Polasik, M.D. Uchic, M.J. Mills, Dislocation structures and their relationship to strength in deformed nickel microcrystals, Acta Mater. 56 (13) (2008) 2988–3001, http://dx.doi.org/10.1016/J.ACTAMAT.2008.02.046.

[38] J.D. Eshelby, The equation of motion of a dislocation, Phys. Rev. 90 (2) (1953) 248–255, http://dx.doi.org/10.1080/01418618308245257.

[39] J.D. Eshelby, The interaction of kinks and elastic waves, Proc. R. Soc. Lond. Ser. A Math. Phys. Sci. 266 (1325) (1962) 222–246, http://dx.doi.org/10.1098/rspa.1962.0058.

[40] A. Kosevich, Dynamical theory of dislocations, Uspekhi Fizicheskih Nauk 84 (12) (1964) 579–609, http://dx.doi.org/10.3367/ufnr.0084.196412c.0579.

[41] R.M. Fisher, J.S. Lally, Microplasticity detected by an acoustic technique, Can. J. Phys. 45 (2) (1967) 1147–1159, http://dx.doi.org/10.1139/p67-084.

[42] A. Agarwal, An investigation of the behavior of the acoustic emission from metals and a proposed mechanism for its generation, 1968.

[43] R.T. Sedgwick, Acoustic emission from single crystals of LiF and KCl, J. Appl. Phys. 39 (3) (1968) 1728–1740, http://dx.doi.org/10.1063/1.1656422.

[44] V. Natsik, A. Burkanov, Radiation of Rayleigh waves by an edge dislocation emerged on crystal surface, Fizika Tverdogo 14 (5) (1972) 1289–1296.

[45] B.H. Schofield, Research on the sources and characteristics of acoustic emission, in: ASTM STP 505, 1972, p. 11, http://dx.doi.org/10.1520/STP35378S.

[46] N. Kiesewetter, Acoustic emission from moving dislocations, Scr. Metall. 8 (3) (1974) 249–252, http://dx.doi.org/10.1016/0036-9748(74)90247-6.

[47] V. Natsik, K. Chishko, Dynamics and sound radiation of dislocation frank-read source, Fizika Tverdogo 17 (1) (1975) 342–345.

[48] D. Rouby, P. Fleischmann, P.F. Gobin, An acoustic emission source model based on dislocation movement, Intern. Frict. Ultrason. Attenuation (1977) 811.

[49] V. Natsik, K. Chishko, Acoustic emission from dislocations moving near the surface of a crystal, Fizika Tverdogo 20 (2) (1978) 457–465.

[50] C.B. Scruby, J.C. Collingwood, H.N. Wadley, A new technique for the measurement of acoustic emission transients and their relationship to crack propagation, J. Phys. D: Appl. Phys. 11 (17) (1978) 2359–2369, http://dx.doi.org/10.1088/0022-3727/11/17/007.

[51] J. Simmons, R. Clough, M. Ashby, R.B.P.I. Conf., U. U. Gainesville, Dislocation modelling of physical systems, 1981, 1980, http://dx.doi.org/10.1016/c2013-0-03471-8.

[52] D. Rouby, P. Fleischmann, C. Duvergier, Un modèle de sources d'émission acoustique pour l'analyse de l'émission continue et de l'émission par salves I. Analyse théorique, Phil. Mag. A 47 (5) (1983) 671–687, http://dx.doi.org/10.1080/01418618308245257.

[53] W. Schaarwächter, H. Ebener, Acoustic emission: A probe into dislocation dynamics in plasticity, Acta Metall. Mater. 38 (2) (1990) 195–205, http://dx.doi.org/10.1016/0956-7151(90)90049-M.

[54] A. Trochidis, B. Polyzos, Acoustic emission during plastic deformation of crystals: A lattice-dynamics approach, J. Appl. Phys. 78 (1) (1995) 170–175, http://dx.doi.org/10.1063/1.360648.

[55] N.I. Tymiak, A. Daugela, T.J. Wyrobek, O.L. Warren, Highly localized acoustic emission monitoring of nanoscale indentation contacts, J. Mater. Res. 18 (4) (2003) 784–796, http://dx.doi.org/10.1557/JMR.2003.0109.

[56] M.C. Miguel, A. Vespignani, S. Zapperi, J. Weiss, J.R. Grasso, Intermittent dislocation flow in viscoplastic deformation, Nature 410 (6829) (2001) 667–671, http://dx.doi.org/10.1038/35070524.

[57] J. Weiss, T. Richeton, F. Louchet, F. Chmelik, P. Dobron, D. Entemeyer, M. Lebyodkin, T. Lebedkina, C. Fressengeas, R.J. McDonald, Evidence for universal intermittent crystal plasticity from acoustic emission and high-resolution extensometry experiments, Phys. Rev. B 76 (22) (2007) 224110, http://dx.doi.org/10.1103/PhysRevB.76.224110.

[58] W. Sikorski, Acoustic emission - Research and applications, InTech (2013) http://dx.doi.org/10.5772/50270.

[59] D. Rouby, P. Fleischmann, C. Duvergier, Un modèle de sources d'émission acoustique pour l'analyse de l'émission continue et de l'émission par salves II. Vérifications expérimentales, Phil. Mag. A 47 (5) (1983) 689–705, http://dx.doi.org/10.1080/01418618308245258.

[60] J. Weiss, F. Lahaie, J.R. Grasso, Statistical analysis of dislocation dynamics during viscoplastic deformation from acoustic emission, J. Geophys. Res. Solid Earth 105 (B1) (2000) 433–442, http://dx.doi.org/10.1029/1999JB900312.

[61] V. Natsik, K. Chishko, Sound radiation during the annihilation of dislocations, Fizika Tverdogo 14 (11) (1972) 3126–3132.

[62] N. Kiesewetter, P. Schiller, The acoustic emission from moving dislocations in aluminium, Phys. Status Solidi (a) 38 (2) (1976) 569–576, http://dx.doi.org/10.1002/pssa.2210380218.

[63] J.D. Eshelby, Dislocations as a cause of mechanical damping in metals, Proc. R. Soc. Lond. Ser. A Math. Phys. Sci. 197 (1050) (1949) 396–416, http://dx.doi.org/10.1098/rspa.1949.0072.

[64] A. Granato, K. Lücke, Theory of mechanical damping due to dislocations, J. Appl. Phys. 27 (6) (1956) 583–593, http://dx.doi.org/10.1063/1.1722436.

[65] A. Vinogradov, A.V. Danyuk, D.L. Merson, I.S. Yasnikov, Probing elementary dislocation mechanisms of local plastic deformation by the advanced acoustic emission technique, Scr. Mater. 151 (2018) 53–56, http://dx.doi.org/10.1016/j.scriptamat.2018.03.036.

[66] A. Vinogradov, I.S. Yasnikov, D.L. Merson, Phenomenological approach towards modelling the acoustic emission due to plastic deformation in metals, Scr. Mater. 170 (2019) 172–176, http://dx.doi.org/10.1016/j.scriptamat.2019.06.011.

[67] B. Devincre, T. Hoc, L. Kubin, Dislocation mean free paths and strain hardening of crystals, Science 320 (5884) (2008) 1745–1748, http://dx.doi.org/10.1126/science.1156101.

[68] S.I. Rao, C. Woodward, B. Akdim, E. Antillon, T.A. Parthasarathy, J.A. El-Awady, D.M. Dimiduk, Large-scale dislocation dynamics simulations of strain hardening of Ni microcrystals under tensile loading, Acta Mater. 164 (2019) 171–183, http://dx.doi.org/10.1016/j.actamat.2018.10.047.

[69] A.M. Hussein, S.I. Rao, M.D. Uchic, D.M. Dimiduk, J.A. El-Awady, Microstructurally based cross-slip mechanisms and their effects on dislocation microstructure evolution in fcc crystals, Acta Mater. 85 (2015) 180–190, http://dx.doi.org/10.1016/j.actamat.2014.10.067.